Doping by Design: Enhanced Thermoelectric Performance of GeSe Alloys Through Metavalent Bonding

Yuan Yu, Chongjian Zhou,* Tanmoy Ghosh, Carl-Friedrich Schön, Yiming Zhou, Sophia Wahl, Mohit Raghuwanshi, Peter Kerres, Christophe Bellin, Abhay Shukla, Oana Cojocaru-Mirédin, and Matthias Wuttig*

Doping is usually the first step to tailor thermoelectrics. It enables precise control of the charge-carrier concentration and concomitant transport properties. Doping should also turn GeSe, which features an intrinsically a low carrier concentration, into a competitive thermoelectric. Yet, elemental doping fails to improve the carrier concentration. In contrast, alloying with Ag–V–VI$_2$ compounds causes a remarkable enhancement of thermoelectric performance. This advance is closely related to a transition in the bonding mechanism, as evidenced by sudden changes in the optical dielectric constant ε_∞, the Born effective charge, the maximum of the optical absorption $\varepsilon_2(\omega)$, and the bond-breaking behavior. These property changes are indicative of the formation of metavalent bonding (MVB), leading to an octahedral-like atomic arrangement. MVB is accompanied by a thermoelectric-favorable band structure featuring anisotropic bands with small effective masses and a large degeneracy. A quantum-mechanical map, which distinguishes different types of chemical bonding, reveals that orthorhombic GeSe employs covalent bonding, while rhombohedral and cubic GeSe utilize MVB. The transition from covalent to MVB goes along with a pronounced improvement in thermoelectric performance. The failure or success of different dopants can be explained by this concept, which redefines doping rules and provides a "treasure map" to tailor p-bonded chalcogenides.

1. Introduction

The demand for sustainable and clean energy has motivated the development of thermoelectric (TE) materials, which can directly convert heat into electricity and enable distributed cooling.[1–3] The efficiency of energy conversion is measured by the dimensionless figure of merit, $zT = S^2\sigma T/(\kappa_{ele} + \kappa_{lat})$, where S, σ, T, κ_{ele}, and κ_{lat} are the Seebeck coefficient, electrical conductivity, absolute temperature, electronic thermal conductivity, and lattice thermal conductivity, respectively.[4–8] Even though the expression for zT appears simple, increasing its value is a formidable task. Specifically, while a high S is often obtained in semiconductors, a large σ is found in metals, and a low κ_{lat} is realized in amorphous materials.[6,9] This is already indicative of complex optimization requirements. Obviously, the relevant optimization parameters S, σ, and κ_{ele} are closely intertwined. This impedes the improvement of zT and the identification of superior thermoelectrics. Hence, the

Y. Yu, T. Ghosh, C.-F. Schön, Y. Zhou, S. Wahl, M. Raghuwanshi,
P. Kerres, O. Cojocaru-Mirédin, M. Wuttig
Institute of Physics (IA)
RWTH Aachen University
Sommerfeldstraße 14, 52074 Aachen, Germany
E-mail: wuttig@physik.rwth-aachen.de
C. Zhou
State Key Laboratory of Solidification Processing
and Key Laboratory of Radiation Detection Materials and Devices
Ministry of Industry and Information Technology
Northwestern Polytechnical University
Xi'an 710072, P. R. China
E-mail: cjzhou@nwpu.edu.cn

P. Kerres, M. Wuttig
PGI 10 (Green IT)
Forschungszentrum Jülich GmbH
52428 Jülich, Germany
C. Bellin, A. Shukla
Institut de Minéralogie
de Physique des Matériaux et de Cosmochimie
Sorbonne Université
UMR CNRS 7590
MNHN
4 Place Jussieu, Paris F-75005, France
M. Wuttig
Jülich – Aachen Research Alliance (JARA-FIT and JARA-HPC)
RWTH Aachen University
52056 Aachen, Germany

development of straightforward and comprehensible optimization strategies could provide much-needed thrust.

Indeed, the last decades have witnessed the development of several such strategies.[10–15] As early as 1956, Ioffe et al. proposed that solid solutions or alloys should be superior to pure elements or compounds for TE applications.[1,16] In line with this suggestion, the TE properties in classic systems such as Bi_2Te_3, PbTe, and Si could be significantly improved by doping/alloying with Sb, Se, and Ge, respectively.[17] Since then, the chemical doping strategy has been employed extensively to optimize TE performance. The most obvious purpose of doping is to adjust the charge-carrier concentration by donating or accepting electrons. Yet, doping can also suppress thermal conductivity by introducing defects.[1,17,18] With the development of rigorous theories and a better understanding of the impact of the electronic band structure, the chemical doping strategy has been further refined. It now enables band engineering to improve power factors by tuning the density-of-states and the band effective masses.[19,20] Taking PbTe as an example, the band convergence with aligned band extrema is realized by doping with Se,[11] Eu,[21] and Mg;[22] and the band anisotropy with different longitudinal and transverse band effective masses can be modified by doping with Mn.[23] Similarly, the TE performance of GeTe can be largely improved by doping with Sb,[24] In,[24] Bi,[25] Pb,[25,26] Mn,[27] Cd,[28] etc. It seems that chemical doping is a universal approach to increase zT. It thus should be easily applicable to all other TE materials, including Cu-doped PbSe,[29] Sn-doped PbS,[30] In-doped SnTe,[31] and Na/Br-doped SnSe,[32,33] to name a few. However, the elemental doping strategy inexplicably fails to adjust the carrier concentration and TE properties of some compounds. GeSe is such an example, as will be elaborated below.

As a close isoelectronic counterpart to GeTe and SnSe, GeSe has attracted much less attention because of its poor TE performance. Theoretical calculations predicted very promising TE properties for GeSe with an optimized carrier concentration of about 5×10^{19} cm^{-3}.[34] Intuitively, it should be easy to tune the carrier concentration by conventional chemical doping because it works efficiently in other IV–VI chalcogenides as summarized above. Yet, extensive work demonstrates that it is very difficult to increase the carrier concentration in GeSe by dopants such as Na,[35–37] Cu,[37] Ag,[35,37] Bi,[37] Sb,[38] La,[37] As,[37] and I.[37] The highest carrier concentration achieved by Ag/Sn co-doping (10^{18} cm^{-3})[37] is still far below the optimum value for GeSe.[34] As a result, a maximum zT of only 0.2 was obtained in $Ag_{0.01}Ge_{0.79}Sn_{0.2}Se$.[37] In striking contrast, the carrier concentration of GeSe can be easily increased by orders of magnitude upon alloying with GeTe,[39–41] Sb_2Te_3,[42] $AgSbSe_2$,[43] $AgSbTe_2$,[44] $AgBiSe_2$,[45,46] and $AgBiTe_2$.[47] As a consequence, the zT value is increased by a factor of about ten (to $zT \approx 1.0$) compared to pristine GeSe ($zT < 0.1$).[40,42–47] This dichotomy into successful and unsuccessful dopants is striking, in particular since it seems difficult to explain the difference between success and failure. Hence, it is fair to say that clear selection criteria for dopants of a given solid are still missing.

In this work, GeSe–x%$AgSbSe_2$ alloys ($x = 0, 2.5, 5, 7.5, 10,$ and 15) are selected as representative samples to reveal the mechanism underpinning the successful doping of Ag–V–VI_2 compounds in GeSe. This study shows that there is a common denominator found for all successful dopants. In the second step, it will be shown that this common denominator can be attributed to an unconventional bonding mechanism. In the third part, the close relationship between the favorable TE properties of successfully doped GeSe and its bonding mechanism will be presented. It will be shown that a suitable combination of host and dopant can be predicted from a quantum-chemical map for bonding. This work hence provides a generic avenue to screen dopants with a "treasure map" to tailor the TE properties of chalcogenides.

2. Results and Discussion

Figure 1a shows that the electrical conductivity increases with increasing $AgSbSe_2$ content. Yet, a considerable increase is only obtained when x ≥ 10. Specifically, sample $x = 15$ shows an electrical conductivity of ≈200 S cm^{-1} in the entire temperature range measured. Note that the hump between 500 and 650 K results from the transition from the rhombohedral to the cubic phase as evidenced by X-ray diffraction (XRD) and differential scanning calorimetry (DSC).[43] Similar phenomena have also been observed in other GeSe–$AgVVI_2$ alloys[43,46] and GeTe[26] upon this phase transition. The Seebeck coefficient for pristine GeSe reaches ≈750 μV K^{-1} over a very large temperature range as shown in Figure 1b. This is due to the extremely low carrier concentration as determined by Hall measurements (3.5×10^{15} cm^{-3}). By introducing $AgSbSe_2$ into GeSe, the Seebeck coefficient decreases to ≈200 μV K^{-1}, falling into the golden range.[48] Due to the significantly increased electrical conductivity and relatively large Seebeck coefficients, sample $x = 15$ shows much higher power factors reaching ≈10.6 μW cm^{-1} K^{-2} between 550 and 725 K, Figure 1c. The total thermal conductivity of pristine GeSe is 2.06 W m^{-1} K^{-1} at room temperature (Figure 1d), in good agreement with the literature data.[37,38,45] Alloying with $AgSbSe_2$ lowers the room-temperature κ_{tot} to ≈1.2 W m^{-1} K^{-1}. The lattice thermal conductivity is calculated by subtracting the electronic contribution according to the Wiedemann–Franz law, $\kappa_{ele} = L\sigma T$, where the Lorenz number L is derived from the Single Parabolic Band (SPB) model (κ_{ele} and thermal diffusivity are provided in Figure S1, Supporting Information). The lattice thermal conductivity (κ_{lat}) decreases with increasing temperature in pristine GeSe. This is characteristic for samples dominated by Umklapp phonon scattering. The $AgSbSe_2$-alloyed samples, on the contrary, exhibit a much smaller temperature dependence, Figure 1e. Particularly for sample $x = 15$, the κ_{lat} is considerably reduced at low temperatures, indicating modifications to the physical parameters that determine κ_{lat}.[8] The small hump in the κ_{lat} curves is induced by the phase transition. Owing to the high power factor and low thermal conductivity, the zT value for sample $x = 15$ is significantly increased in the entire temperature range relative to other samples investigated, Figure 1f. The highest zT value reaches 0.84 at 720 K for sample $x = 15$, which is enhanced by a factor of 12 compared with that for pristine GeSe (0.07 at 720 K). This considerable improvement of zT requires explanations from a perspective of phonon and electron transport, which will be discussed in detail later.
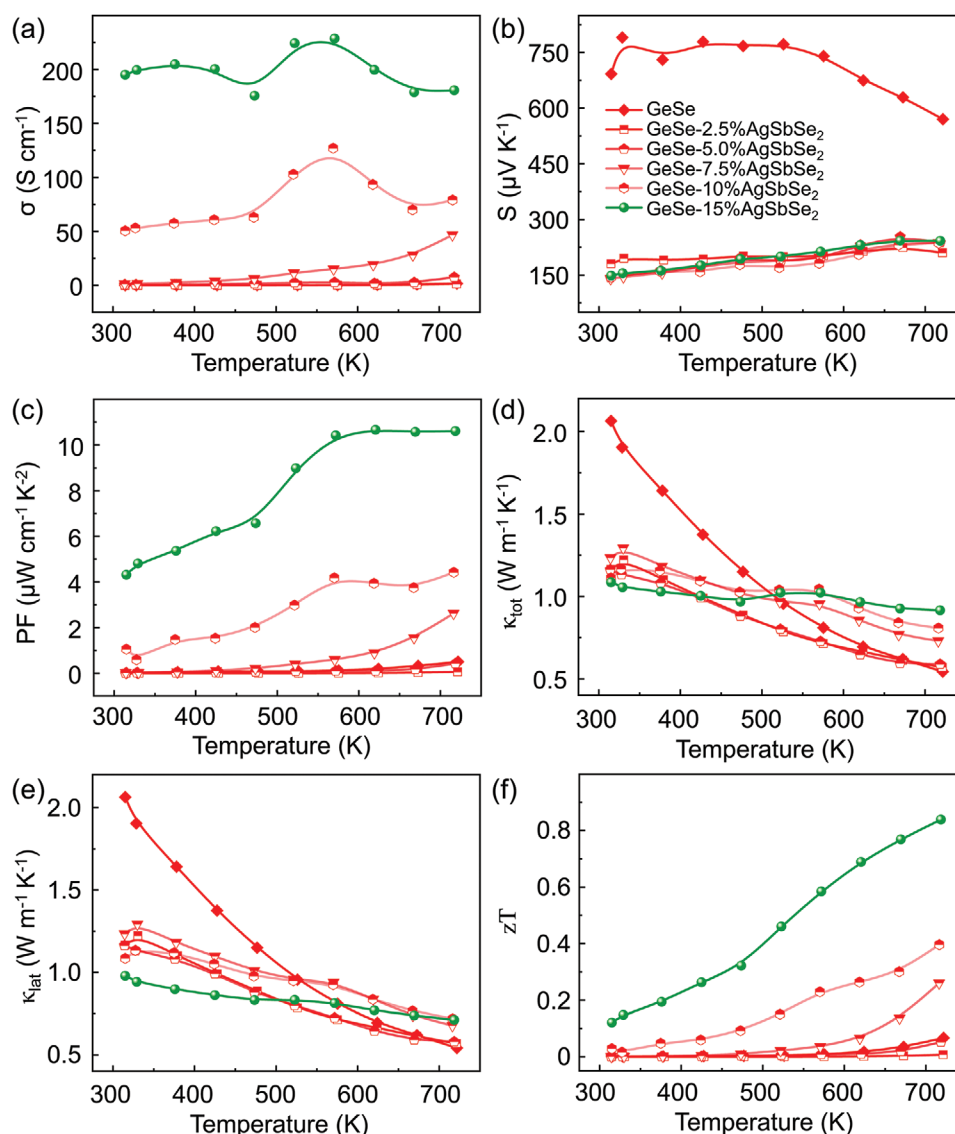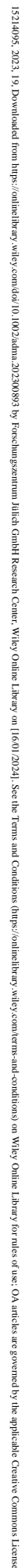
2300893 (2 of 11)

Figure 1. Temperature-dependent thermoelectric properties of GeSe-*x* at% AgSbSe$_2$ alloys (*x* = 0, 2.5, 5, 7.5, 10, and 15). a) Electrical conductivity; b) Seebeck coefficient; c) power factor; d) total thermal conductivity; e) lattice thermal conductivity; and f) figure of merit *zT*.

The TE properties obtained in this work are consistent with that reported by Huang et al.[43] A similar improvement of TE performance has been observed upon alloying with GeTe,[39–41] Sb$_2$Te$_3$,[42] AgSbTe$_2$,[44] AgBiSe$_2$[45,46] and AgBiTe$_2$.[47] This raises the question if there is a common denominator that characterizes all of these dopants. A closer inspection of all these successful dopants reveals that they resemble each other in terms of their atomic arrangement. They display an octahedral atomic arrangement with small or no lattice distortion. This atomic arrangement can be attributed to a special bonding mechanism. All these solids are characterized by half-filled σ-bonds formed of p-orbitals, a bonding configuration that could be described as 2c−1e, that is, metavalent bonding (MVB).[49,50] This bond differs significantly from conventional covalent bonding (2c−2e bonding). Recently, a conceptually simple scheme has been suggested to describe how valence electrons of different atoms interact with each other. Two quantities are sufficient to describe

the bonds between adjacent atoms, that is, the number of electrons transferred (ET) and shared (ES).[49] **Figure 2** shows a 2D map spanned by ET and ES, which are calculated by quantum-chemical tools.[51–53] Interestingly, materials that employ different chemical bonds are located in different regions of the map.[49,54] A pure ionic bond should have an ET value, renormalized by its formal oxidation state of the atoms involved, close to one. On the contrary, a pure covalent bond has an ES value of two, approaching the limit of an electron pair as suggested by Gilbert Lewis.[55] We note that the majority of semiconductors lie on the connecting line between ionic and covalent bonds. Such bonds can be called iono-covalent bonds.[56] The relative size of ES and ET characterizes the contribution of covalent and ionic bonding. Metallic bonds are found in the lower left corner. This region is characterized by small or vanishing ET and a small value for ES, due to a large number of nearest neighbors to share electrons with. Interestingly, the
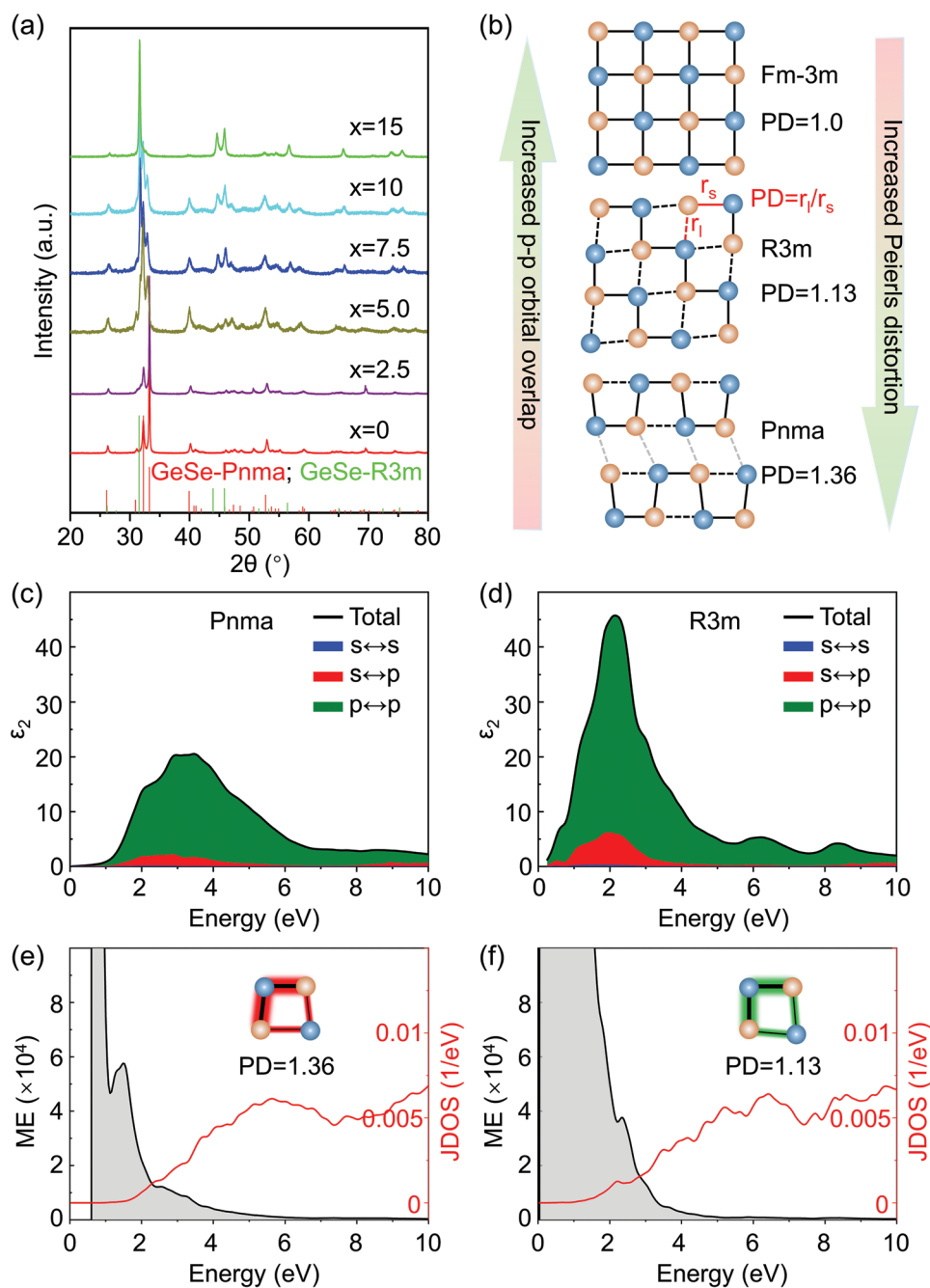
**ADVANCED
SCIENCE NEWS**

www.advancedsciencenews.com

**ADVANCED
MATERIALS**

www.advmat.de

Figure 2. 2D map spanned by the number of electrons transferred, renormalized by the oxidation state (ET), and the number of electrons shared (ES) between adjacent atoms. This map demarcates different chemical bonding mechanisms as depicted by different colors, which are based on the different properties of the different materials. Data are adapted from refs. [49,54], except for rhombohedral and cubic GeSe (this work).

abovementioned compounds that can effectively improve the TE performance of GeSe, such as GeTe, Sb_2Te_3, and $AgSbTe_2$, are all located in a region characterized by a value of ES ≈ 1 and small ET (green area of Figure 2). Moreover, these compounds show a unique property portfolio including a large optical dielectric constant (ε_∞), a high Born effective charge (Z^*), strong anharmonicity, etc.[6,50] This unconventional combination of properties differentiates the corresponding chemical bonding mechanism from metallic, covalent, and ionic bonding and has thus coined metavalent bonding (MVB).[6,49,50,57–60] Concerning thermoelectrics, this raises an important question: why can the TE performance of GeSe be effectively improved through alloying with MVB compounds but not by conventional elemental doping? Understanding this question could accelerate the discovery and design of high-performance TE materials.

In previous studies,[40,41,43–46,61] the considerably enhanced zT in GeSe alloys was attributed to a phase transition from an orthorhombic to a rhombohedral or a cubic phase. Yet, the arrangement of atoms is inherently determined by the chemical bonding mechanism, which governs the structure with the lowest energy. In other words, chemical bonding determines the resulting crystal structure. To provide a chemical bonding perspective on the TE performance, we have calculated the ES and ET values for orthorhombic, rhombohedral, and cubic GeSe as well as some relevant properties related to bonding. The orthorhombic GeSe lies close to the connecting line and employs covalent bonding with an ionic contribution, which is highlighted by a blue circle in Figure 2. In contrast, both rhombohedral and cubic GeSe phases reside in the MVB area. They have been marked by red and violet circles, respectively. Figure 2 provides strong evidence that the poor TE performance of pristine GeSe stems from its covalent bonds. The significant improvement of zT in the GeSe–15%$AgSbSe_2$ alloy, on the contrary, results from the establishment of metavalent bonds. In the following, we will prove that the transition from covalent to metavalent bonds is essential for significantly improved TE

properties. Subsequently, it will be explained, why metavalent bonding is favorable for the TE properties of many chalcogenides and related materials.

Figure 3a presents the X-ray diffraction (XRD) patterns, which indicate that pristine GeSe and sample $x = 2.5$ employ an orthorhombic crystal structure (Pnma), while samples $x = 5$, 7.5, and 10 possess a mixture of orthorhombic and rhombohedral (R3m) phases. In contrast, sample $x = 15$ can be indexed to a pure R3m phase without a discernible second phase. All the abovementioned MVB compounds highlighted by yellow circles in Figure 2 will drive the phase transition from orthorhombic GeSe toward rhombohedral or cubic GeSe upon doping with these compounds. Figure 3b schematically sketches the transformation between these three phases. Both the rhombohedral and orthorhombic structures can be derived from the cubic one. The transition from cubic to rhombohedral and finally orthorhombic GeSe can be attributed to a reduced degree of p-orbital overlap and a concomitant increase of the Peierls distortion (PD), where PD $= r_l/r_s$, that is, the ratio between long and short bonds, as indicated in Figure 3b. The size of the PD is governed by the two quantum chemical bonding descriptors ES and ET.[54] Materials lying on the dashed green line in Figure 2 have no PD but instead, show a perfect octahedral arrangement. Solids in the green region above the green dashed line, that is, materials with a larger ES value, possess a PD, which increases with increasing ES value. These materials have a distorted octahedral arrangement, yet with rather moderate PD values. They frequently show a rhombohedral structure. Upon the transition from the metavalent to the covalent region, the chalcogenides discussed here, that is, GeSe or also SnSe, experience a significant change in atomic arrangement and switch to an orthorhombic arrangement. This rearrangement leads to a much smaller overlap of adjacent p-orbitals, with several concomitant property changes. This can be seen from the optical dielectric function $\varepsilon(\omega)$, in particular the imaginary part $\varepsilon_2(\omega)$.

**ADVANCED
SCIENCE NEWS**

www.advancedsciencenews.com

**ADVANCED
MATERIALS**

www.advmat.de

Figure 3. Correlations between phase transition and p-orbital overlap. a) XRD patterns at room temperature showing the pristine orthorhombic GeSe and a rhombohedral phase for GeSe–15%AgSbSe$_2$, as well as the mixture of both between them for intermediate compositions. b) Sketches of cubic (Fm-3), rhombohedral (R3m), and orthorhombic (Pnma) GeSe phases, illustrating how the various structures derive from the cubic one by decreasing the p–p orbital overlap and thus increasing the degree of Peierls distortion. c,d) Orbital-resolved energy dependence of the imaginary part of the dielectric function for Pnma GeSe (c) and for R3m GeSe (d). e,f) Energy-dependent matrix element (ME) and joint density of states (JDOS) for Pnma GeSe (e) and for R3m GeSe (f).

Figure 3c,d shows the orbital-resolved imaginary part of the dielectric function ($\varepsilon_2(\omega)$) in the energy range of electronic interband transitions obtained by density functional theory (DFT) calculations for Pnma and R3m GeSe phases, respectively (data for Fm-3m phase can be found in Figure S2, Supporting Information). The orbital-resolved $\varepsilon_2(\omega)$ demonstrates that the strong optical absorption primarily stems from the p–p

interband transitions for three GeSe phases. Yet, the maximum of $\varepsilon_2(\omega)$ shifts toward lower energies and increases in magnitude upon the phase transition from the orthorhombic to the rhombohedral and then to the cubic phase (Figure S2a, Supporting Information). According to Fermi's golden rule, the energy dependence of $\varepsilon_2(\omega)$ is governed by the joint density of states (JDOS) stemming from the valence and conduction

ADVANCED
SCIENCE NEWS
www.advancedsciencenews.com

ADVANCED
MATERIALS
www.advmat.de

band energies, and by the matrix element for the transition between these states. Figure 3e,f indicates that the JDOS does not change significantly for the different phases. In contrast, the matrix element is considerably larger for the R3m phase. A non-vanishing matrix element is obtained when the parity of the initial and the final state changes. The size of the matrix element depends on the degree of orbital overlap. An increase in p–p orbital overlap, which characterizes a decreasing size of the Peierls distortion results in the enlarged matrix elements in the R3m phase (and Fm-3m phase). Due to the optical sum rule, this leads to a shift of the maximum of $\varepsilon_2(\omega)$ to lower energies. Therefore, we can conclude that the phase transition from Pnma to R3m and then to Fm-3m is dominated by the increasing degree of p–p orbital overlap. This change in bonding also modifies the corresponding electronic band structures and concomitant transport properties as will be discussed below.

To validate that the change in structure is indeed accompanied by a change in bonding, atom probe tomography (APT) studies have been performed. APT works on the principle of field evaporation.[18,62] Surface atoms evaporate in a high electric field by breaking the bonds to neighboring atoms triggered by a short laser pulse. Note that APT is sensitive to the bonds rather than the arrangement of atoms, that is, the crystal structure. Different chemical bonds show a distinct bond-rupture behavior. This is especially true for metavalent bonds, which are characterized by a rather unconventional bond rupture, characterized by exceptionally high values for the probability of multiple events (PME).[6,57,63,64] These multiple events describe the evaporation of more than one ion dislodged by a successful laser pulse (an unsuccessful laser pulse does not produce any detected ion dislodgement).[57,65] PME values >60% have been observed for all MVB compounds studied so far, as plotted in **Figure 4**b.[6,57,63,64] PME values significantly <60% are characteristic for the other bonding mechanisms discussed here, that is, ionic and covalent bonding. Figure 4a shows the PME map of three GeSe samples with different AgSbSe$_2$ content, $x = 0$, 10, 15. The low PME value (30%) for pristine GeSe corroborates its covalent bonding nature. In contrast, the high PME value (72%) for the $x = 15$ sample is indicative of MVB. We note that sample $x = 10$ contains different regions, which show strikingly dissimilar PME values. Interestingly, these two parts also show different chemical compositions. Figure 4c depicts the composition profile across the interface from the low-PME region to the high-PME region. While one phase shows a very low content of Ag and Sb, the other phase is enriched in Ag and Sb and depleted in Ge. The corresponding PME profile from top to bottom confirms that the Ag/Sb-poor phase is the covalent Pnma GeSe matrix, while the Ag/Sb-rich phase is the MVB R3m GeSe–15%AgSbSe$_2$ alloy (Figure 4d). This phenomenon of phase separation (see also XRD data in Figure 3a) with distinct PME values for each phase is observed in samples from $x = 2.5$ to 10 (Figures S3–S8, Supporting Information). Repetitive measurements confirm that the solubility of Ag and Sb in the orthorhombic GeSe matrix is ≈1.0 at% regardless of the AgSbSe$_2$ content of the sample. This demonstrates a low solubility limit of Ag and Sb in orthorhombic GeSe, consistent with the observation that Ag or Sb alone cannot be efficiently doped into GeSe.[37] The second phase observed also
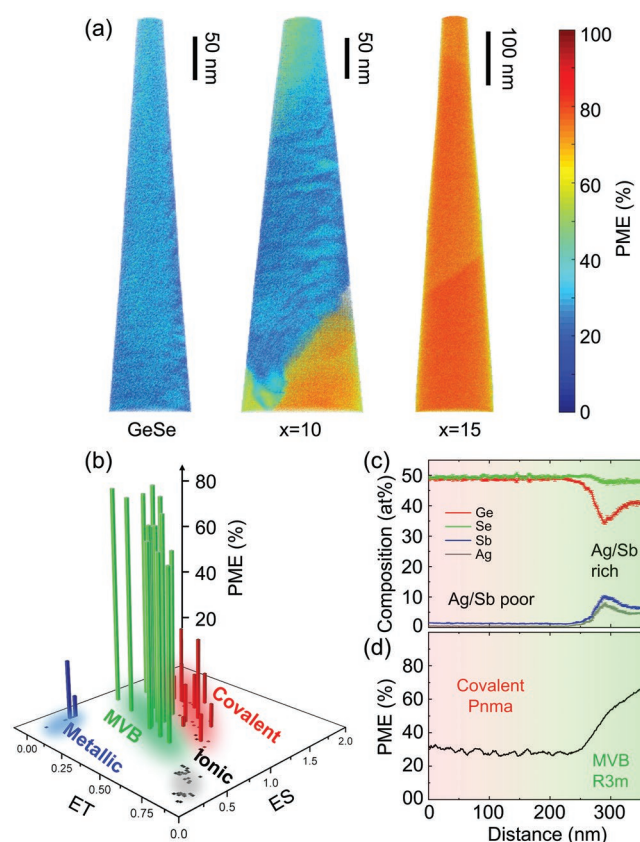

Figure 4. Bond breaking in APT measurements for different GeSe phases. a) 3D PME plot for samples GeSe, $x = 10$ and 15. While a low PME value is observed in GeSe, a high PME is observed in $x = 15$ and phase separation occurs in $x = 10$. Note that the slightly different PME values in sample $x = 15$ are induced by the variations of the local electric field along different crystallographic planes.[65] b) PME values plotted on the basal plane of the ES-ET map as shown in Figure 2. A large PME value is characteristic for all MVB compounds. c) 1D composition profile along the vertical axis of sample $x = 10$ across the phase boundary. d) PME profile from top to bottom; the Ag/Sb-poor area shows low PME value corresponding to the covalent bonding (Pnma phase) while the Ag/Sb-rich area shows high PME value corresponding to the metavalent bonding (R3m phase). b) Adapted with permission.[6] Copyright 2019, The Authors, published by Wiley-VCH.

shows a very similar composition and high PME value for all samples. XRD results show a mixture of orthorhombic and rhombohedral phases in samples from $x = 2.5$ to 10, while a pure orthorhombic GeSe and a pure rhombohedral GeSe–15%AgSbSe$_2$ phase are observed for the two end members. If the AgSbSe$_2$ content is above the solubility limit of Ag and Sb in GeSe (1%), the structure can no longer be stabilized in the pure orthorhombic phase because it cannot accommodate such a high AgSbSe$_2$ content. Yet, a pure rhombohedral phase can only be formed when the AgSbSe$_2$ content is high enough. Thus, phase separation occurs in samples from $x = 2.5$ to 10 as observed by XRD and APT. The abrupt transition from covalent bonding to MVB is consistent with the discontinuity in Peierls distortion and property changes between covalent and MVB compounds.[54,66] Besides the distinctly different bond rupture, the optical properties also show considerable differences

**ADVANCED
SCIENCE NEWS**

www.advancedsciencenews.com

**ADVANCED
MATERIALS**

www.advmat.de

between the pristine GeSe and the GeSe–15%AgSbSe$_2$ alloy. The optical dielectric constant (ε_∞), which describes the electronic polarizability, increases from 16.1 for GeSe to 26.7 for the rhombohedral GeSe–15%AgSbSe$_2$ alloy. These are close to the values calculated by DFT, which are 14.4 and 33.5 for the Pnma and R3m GeSe phases, respectively. The enlarged ε_∞ values again are closely related to the large orbital overlap of the R3m phase, as compared to the Pnma phase. In addition, the Born effective charge Z^*, which describes the polarizability of chemical bonds, also increases from 2.6 for the Pnma phase to 4.6 for the R3m phase and then to 8.6 for the Fm-3m phase, as obtained by DFT calculations. These abrupt changes in bonding-related properties and bond-breaking behavior accompany the transition of chemical bonding from covalent to metavalent. So far, we have shown that pristine orthorhombic GeSe employs covalent bonding, while sample $x = 15$ with a rhombohedral structure employs MVB. Samples with intermediate composition possess a mixture of both phases with an increasing fraction of the MVB phase upon increasing AgSbSe$_2$ content. This can also be seen in the energy-dispersive spectroscopy (EDS) results, where the volume fraction of the Ag/Sb-rich phase increases with increasing nominal content of AgSbSe$_2$ (Figures S9–S14, Supporting Information). Hence, it can be summarized that there is a close relationship between the favorable properties of the rhombohedral GeSe phase and its bonding mechanism.

Subsequently, several arguments will be presented, which illuminate why metavalent bonds lead to favorable TE properties. The crucial quantity to optimize the zT value is determined by several intertwined physical parameters, which can be summarized in a so-called B factor (Equation 1) to describe the potential of a material to obtain large zT at the optimized carrier concentration and acoustic phonon dominated carrier scattering mechanism.[67,68]

$$B = \frac{2k_B^2 \hbar T C_l}{3\pi \Xi^2} \frac{N_v^* K^*}{m_\sigma^* \kappa_{lat}} \tag{1}$$

where k_B is the Boltzmann constant, $\hbar$ is the reduced Planck's constant, C_l is the longitudinal elastic constant, and Ξ is the deformation potential. It demonstrates that a small conductivity effective mass (m_σ^*), a low lattice thermal conductivity, and a large Fermi surface complexity factor ($N_v^* K^*$) are beneficial to realize a high zT.

Among these parameters, the lattice thermal conductivity is relatively independent of others and is closely linked to the bond strength and the lattice anharmonicity. The MVB phase has on average about one electron shared between adjacent atoms, corresponding to a bond order of 0.5, which is only half that for the case of an electron pair in covalent GeSe. This leads to lower optical phonon frequencies and larger thermal expansion coefficients. All these factors contribute to soft chemical bonds in the MVB phase and thus a lower phonon group velocity. Besides, the Born effective charge Z^* for the MVB phases ($Z^* = 4.6$ for R3m and $Z^* = 8.6$ for Fm-3m) is considerably larger than that for the pristine covalent GeSe ($Z^* = 2.6$). This leads to a more prominent splitting of the longitudinal optical (LO) and transverse optical (TO) phonons (Lyddane–Sachs–Teller relationship).[69,70] Moreover, the delocalized p-electrons

in the MVB phase cause a strong electron–TO-phonon coupling, leading to phonon softening and strong anharmonic TO modes.[71] These conclusions are also in line with Raman data discussed in Figure S15 (Supporting Information). The large anharmonicity of the rhombohedral GeSe phase is also supported by DFT calculations. A large mode-averaged Grüneisen parameter of 1.83 at room temperature is obtained for the R3m phase,[72] which is comparable to lead chalcogenides.[73] This large anharmonicity is the primary factor giving rise to the low κ_{lat} of the MVB GeSe phase.

The soft metavalent bonds are also favorable to create vacancies that increase the charge-carrier concentration. It has been argued that the poor TE performance of pristine GeSe is due to its intrinsically low carrier concentrations.[34] Upon the bonding transition to MVB, the formation energy of cation vacancies is significantly reduced due to the soft chemical bond, as proved by DFT calculations in Figure S16 (Supporting Information). These cation vacancies provide delocalized holes, that is, holes with small effective masses for charge transport. Hall measurements (Table S1, Supporting Information) show that the carrier concentration increases by 4 orders of magnitude upon the bonding transition from covalent to MVB, leading to the increase in electrical conductivity and the decrease in Seebeck coefficient shown in Figure 1. Yet, the increased carrier concentration alone cannot be fully responsible for the improved TE performance since the electronic properties are also interrelated to the mobility and effective masses of the charge carriers.

Figure 5a shows the orbital-resolved band structures for orthorhombic, rhombohedral (with PD = 1.13, as determined by XRD), and cubic GeSe obtained by DFT calculations. All the conduction and valence bands close to the Fermi energy are dominated by the p states of Ge and Se, which is in line with the argument that the s-lone pairs may not be as crucial as previously thought.[74] We also calculated the angle-resolved hole effective mass at the valence band maximum for these three GeSe phases as shown in Figure S17 (Supporting Information). Thereby, the different effective masses and the band anisotropy (K) for these phases can be obtained, see **Table 1**. According to the $k \cdot p$ perturbation theory, the band effective mass (m_b^*) is inversely proportional to the energy bandgap. **Figure 6**a schematically illustrates the evolution of the bandgap upon the increasing degree of p-orbital overlap. With a half-filled p band, we are expecting a metallic ground state in MVB materials, which are also called incipient metals.[50] Both charge transfer (enlarged ET) and Peierls distortion (enlarged ES) reduce the degree of orbital overlap and thus open the bandgap. As a consequence, the bandgap decreases from Pnma to R3m and then to Fm-3m with increasing p-orbital overlap. Optical measurements show a bandgap of 1.06 eV for pristine GeSe and a much smaller value of 0.32 eV for the rhombohedral phase (sample $x = 15$). This directly results in a reduced m_b^* and thus m_σ^* as well as an increased carrier mobility (μ) in the rhombohedral phase (See Table S1, Supporting Information).

The last parameter that impacts the B value and thus zT is the Fermi surface complexity factor ($N_v^* K^*$), which describes the ability of different energy bands to maximize the power factor. This quantity can be used in high-throughput searches for promising thermoelectrics.[68] The product $N_v^* K^*$ can be divided into two contributions from the valley degeneracy (N_V)
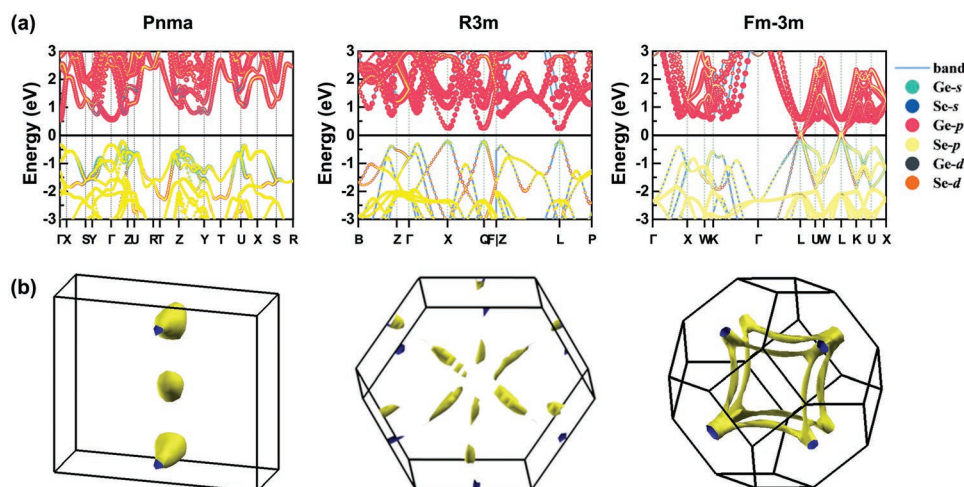
**ADVANCED
SCIENCE NEWS**

www.advancedsciencenews.com

**ADVANCED
MATERIALS**

www.advmat.de

Figure 5. Electronic band structures for different GeSe phases. a) Energy band structures for orthorhombic, rhombohedral (PD = 1.13), and cubic GeSe phases. b) Corresponding constant energy surfaces at a value of −0.3 eV relative to the Fermi energy in the first Brillouin zone for these phases.

and the band anisotropy (K). The constant energy surfaces at a value of −0.3 eV below the Fermi energy in the first Brillouin zone for three GeSe phases are depicted in Figure 5b. The valence band maximum lies in the Γ–Z direction with a valley degeneracy (N_V) of 2 for the orthorhombic phase. An N_V value of 3 can be achieved when the Fermi energy enters deeply into the valence band (e.g., −0.3 eV) reaching the second maximum at the Γ point. However, it is very difficult to realize this high carrier concentration experimentally due to the weak dopability of covalent GeSe.[37] In contrast, the valence band maximum for the cubic phase is located at the L point with an N_V of 4 due to the high symmetry of the Brillouin zone. At a high doping level, the Σ bands with an N_V of 12 can also contribute to the conduction, leading to a total N_V of 16 for cubic GeSe, similar to the case of PbTe.[11,74] The Peierls distortion slightly reduces the symmetry of the Brillouin zone and thus the valley degeneracy. Yet, at least an N_V of 9 is feasible at a reasonable doping level for the rhombohedral phase as shown in Figure 5b. The MVB phases also show a larger band anisotropy than the covalent phase. The large band anisotropy stems from weak s–p hybridization and small ionicity (low ET values),[39] which is a typical feature for MVB compounds such as GeTe,[68] PbTe,[68] and AgBiSe₂.[75] By plotting the $N_V^* K^*$ of three GeSe phases as well as other compounds calculated by Gibbs et al.[68] onto the basal plane of ES and ET, we find a clear trend that the MVB compounds all show a much higher $N_V^* K^*$ and thus a larger power factor than others (Figure 6b; Figure S12, Supporting Information). Moreover, this map even demonstrates the trend of $N_V^* K^*$ with changing ES or ET. For example, the $N_V^* K^*$ decreases from PbTe to PbSe and then to PbS by increasing

the number of ET. In contrast, the $N_V^* K^*$ increases from Pnma to R3m and then to Fm-3m GeSe phases by decreasing the number of ES. Thus, our ES-ET map can also be employed in high-throughput screening of thermoelectrics without calculating the band structures.

3. Conclusions

GeSe was predicted as a promising TE material given an optimum carrier concentration. However, in practice, it is difficult to tune the carrier concentration by conventional doping, even though it should generally work in semiconductors. By alloying with 15% AgSbSe₂, a new GeSe phase with a rhombohedral structure <550 K and a cubic structure >550 K is obtained. These phases show a significantly improved TE performance. As summarized in Figure 6c, APT and optical measurements demonstrate an abnormal bond-breaking behavior, a large optical dielectric constant, and strong optical absorption in this phase. All of these are characteristic fingerprints of metavalent bonding. Compared with covalent GeSe, the MVB phase shows a smaller bandgap, a lower band effective mass, a larger band valley degeneracy, and a higher band anisotropy. As a result, the electrical conductivity and the power factor are considerably enhanced in the MVB phase. Due to the large anharmonicity and softened chemical bonds, the thermal conductivity is also reduced, especially near room temperature. The final maximum zT value is increased by a factor of >10, from 0.07 for pristine GeSe to 0.84 for the GeSe–15%AgSbSe₂ alloy at 720 K. Given the similarities of MVB GeSe to other IV–VI compounds

Table 1. Different effective masses for Pnma, R3m, and Fm-3m GeSe phases obtained by DFT calculations. $m_\perp^*$ and $m_\parallel^*$ are the transverse and longitudinal effective masses, respectively. $K = m_\parallel^*/m_\perp^*$. m_d^* is the density-of-states effective mass and m_e is the free electron mass.

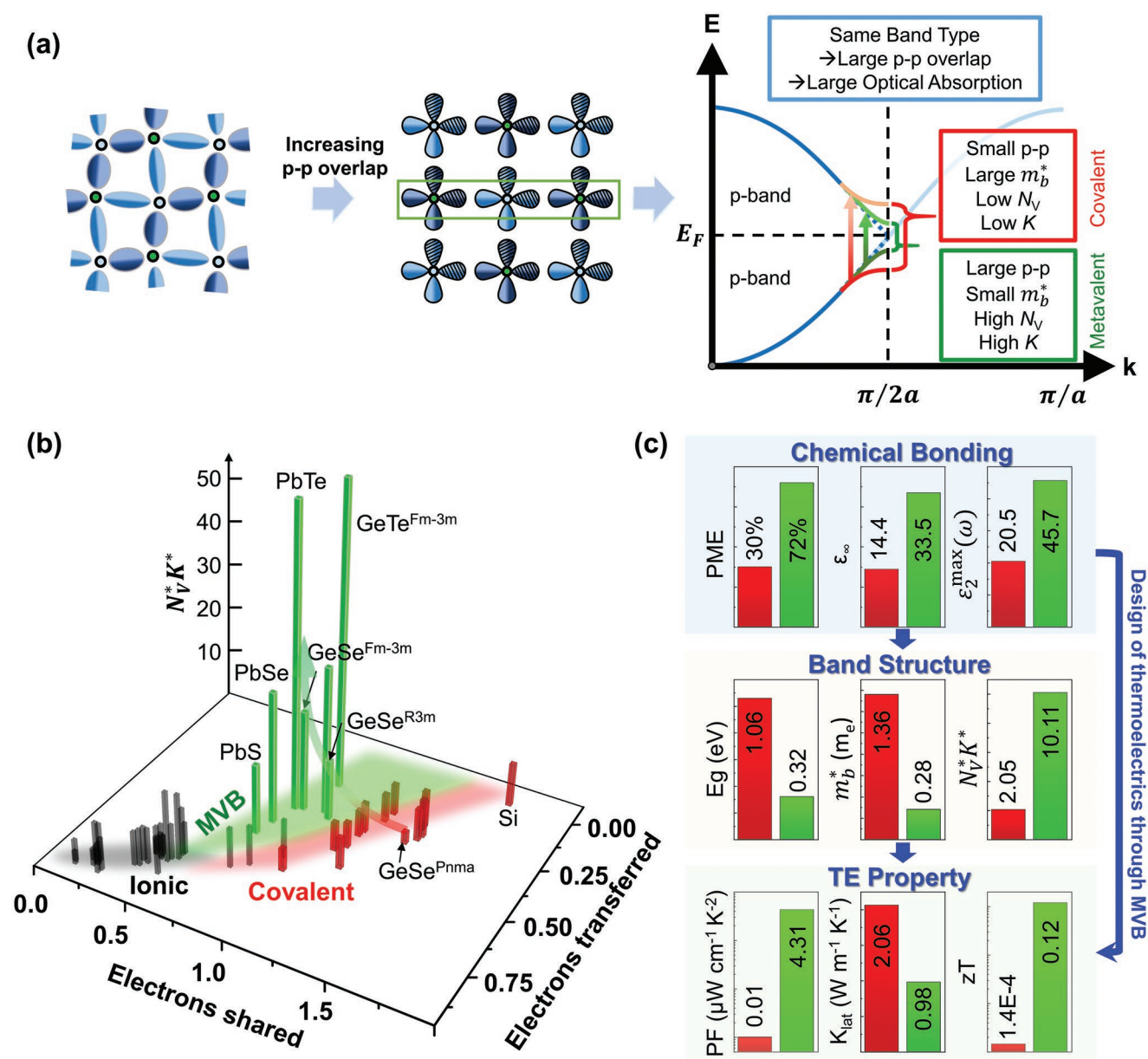| Phases	$m_\parallel^*$	$m_\perp^*$	m_b^*	m_σ^*	N_V	K	m_d^*	$N_V^* K^*$
Pnma	1.75 m_e	1.2 m_e	1.36 m_e	1.34 m_e	2	1.45	2.16 m_e	2.05
R3m	0.51 m_e	0.21 m_e	0.28 m_e	0.26 m_e	9	2.43	1.22 m_e	10.11
Fm-3m	0.08 m_e	0.05 m_e	0.06 m_e	0.06 m_e	16	1.60	0.37 m_e	16.57

Figure 6. Design of thermoelectrics through tailoring chemical bonds. a) Formation of half-filled σ-bonds between p-orbitals of adjacent Ge and Se atoms. Perfectly aligned (half-filled) σ-bonds will result in a metallic ground state. A small charge transfer between Ge and Se opens a small bandgap. The resulting band structure shows a small m_b^*, a high N_V, and a high K. A Peierls distortion can further open the bandgap. This will increase m_b^* and decrease N_V and K. b) The Fermi surface complexity factor of different GeSe phases plotted on the basal plane of ES and ET. Other data points are calculated by Gibbs et al.[68] A large increase in the $N_V^* K^*$ value can be observed upon the transition from Pnma to R3m and then to Fm-3m GeSe phases as indicated by the curved arrow. Compounds in the MVB area show larger $N_V^* K^*$ values. c) Room-temperature properties of pristine GeSe (red bar) and sample GeSe–15% AgSbSe$_2$ (green bar) demonstrating the correlation between chemical bonding and electronic band structures. This close link enables the rational design of thermoelectrics upon tailoring chemical bonds. a) Adapted with permission.[66] Copyright 2021, The Authors, published by Wiley-VCH.

such as GeTe, the zT value can be further improved by fine-tuning the energy band structures and introducing structural defects. Our work describes a new paradigm to design thermoelectrics by tailoring chemical bonds and the resulting electronic band structures upon identifying appropriate dopants. To this end, we have provided a quantum-mechanical map, which is spanned by two quantitative chemical bonding descriptors,

that is, the number of electrons transferred and shared between adjacent atoms. Dopants that turn the bonds metavalent in the compound to be optimized can now easily be identified. This "treasure map" can thus be used to tailor the chemical bonding mechanism and the TE properties of covalent compounds such as GeS and SnSe by crossing the border to enter the metavalent region.

**ADVANCED
SCIENCE NEWS**

www.advancedsciencenews.com

**ADVANCED
MATERIALS**

www.advmat.de

Conflict of Interest

The authors declare no conflict of interest.

Author Contributions

Y.Y., C.Z., and M.W. conceived the project. C.Z. prepared the samples and measured the thermoelectric properties. Y.Y. performed APT measurements. T.G. performed FTIR measurements and data analyses. Y.Z. measured the ellipsometry data. S.W. provided help with the optical measurements. P.K. analyzed the XRD data to fit the value of Peierls distortion. C.-F.S. calculated the ES-ET map. C.Z. calculated the energy band structures and the defect formation energy. M.R., C.B., and A.S. measured the Raman data. Y.Y. constructed the structure, prepared the figures, and wrote the draft. M.W. edited the manuscript. All authors commented on and approved the submission of this work.

Data Availability Statement

The data that support the findings of this study are available from the corresponding author upon reasonable request.

[1] G. S. Nolas, J. Sharp, J. Goldsmid, in *Thermoelectrics: Basic Principles and New Materials Developments*, Vol. *45*, Springer Science & Business Media, Berlin, Germany **2013**.

[2] G. J. Snyder, S. LeBlanc, D. Crane, H. Pangborn, C. E. Forest, A. Rattner, L. Borgsmiller, S. Priya, *Joule* **2021**, *5*, 748.

[3] X.-L. Shi, J. Zou, Z.-G. Chen, *Chem. Rev.* **2020**, *120*, 7399.

[4] G. J. Snyder, E. S. Toberer, *Nat. Mater.* **2008**, *7*, 105.

[5] Z.-G. Chen, G. Han, L. Yang, L. Cheng, J. Zou, *Prog. Nat. Sci.: Mater. Int.* **2012**, *22*, 535.

[6] Y. Yu, M. Cagnoni, O. Cojocaru-Mirédin, M. Wuttig, *Adv. Funct. Mater.* **2020**, *30*, 1904862.

[7] G. Tan, L. D. Zhao, M. G. Kanatzidis, *Chem. Rev.* **2016**, *116*, 12123.

[8] T. Zhu, Y. Liu, C. Fu, J. P. Heremans, G. J. Snyder, X. Zhao, *Adv. Mater.* **2017**, *29*, 1605884.

[9] D. J. Singh, in *Semiconductors and Semimetals* (Ed: T. M. Tritt), Vol. *70*, Elsevier, Amsterdam, The Netherlands **2001**, p. 125.

[10] B. Jiang, Y. Yu, J. Cui, X. Liu, L. Xie, J. Liao, Q. Zhang, Y. Huang, S. Ning, B. Jia, B. Zhu, S. Bai, L. Chen, S. J. Pennycook, J. He, *Science* **2021**, *371*, 830.

[11] Y. Pei, X. Shi, A. LaLonde, H. Wang, L. Chen, G. J. Snyder, *Nature* **2011**, *473*, 66.

[12] S. Roychowdhury, T. Ghosh, R. Arora, M. Samanta, L. Xie, N. K. Singh, A. Soni, J. He, U. V. Waghmare, K. Biswas, *Science* **2021**, *371*, 722.

[13] L. D. Zhao, S. H. Lo, Y. Zhang, H. Sun, G. Tan, C. Uher, C. Wolverton, V. P. Dravid, M. G. Kanatzidis, *Nature* **2014**, *508*, 373.

[14] M. S. Dresselhaus, G. Chen, M. Y. Tang, R. G. Yang, H. Lee, D. Z. Wang, Z. F. Ren, J. P. Fleurial, P. Gogna, *Adv. Mater.* **2007**, *19*, 1043.

[15] J.-D. Musah, A. M. Ilyas, S. Venkatesh, S. Mensah, S. Kwofie, V. A. L. Roy, C.-M. L. Wu, *Nano Res. Energy* **2022**, *1*, e9120034.

[16] A. F. Joffe, S. V. Airapetyants, A. V. Joffe, N. V. Kolomoets, L. S. , *Dokl. Akad. Nauk SSSR* **1956**, *106*, 981.

[17] H. J. Goldsmid, in *Introduction to Thermoelectricity*, Vol. *121*, Springer, Berlin, Germany **2009**.

[18] Y. Yu, C. Zhou, S. Zhang, M. Zhu, M. Wuttig, C. Scheu, D. Raabe, G. J. Snyder, B. Gault, O. Cojocaru-Mirédin, *Mater. Today* **2020**, *32*, 260.

[19] Y. Pei, H. Wang, G. J. Snyder, *Adv. Mater.* **2012**, *24*, 6125.

[20] J. Xin, Y. Tang, Y. Liu, X. Zhao, H. Pan, T. Zhu, *npj Quantum Mater.* **2018**, *3*, 9.

[21] Z. Chen, Z. Jian, W. Li, Y. Chang, B. Ge, R. Hanus, J. Yang, Y. Chen, M. Huang, G. J. Snyder, Y. Pei, *Adv. Mater.* **2017**, *29*, 1606768.

[22] L. D. Zhao, H. J. Wu, S. Q. Hao, C. I. Wu, X. Y. Zhou, K. Biswas, J. Q. He, T. P. Hogan, C. Uher, C. Wolverton, V. P. Dravid, M. G. Kanatzidis, *Energy Environ. Sci.* **2013**, *6*, 3346.

[23] Y. Xiao, H. Wu, J. Cui, D. Wang, L. Fu, Y. Zhang, Y. Chen, J. He, S. J. Pennycook, L.-D. Zhao, *Energy Environ. Sci.* **2018**, *11*, 2486.

[24] M. Hong, Z. G. Chen, L. Yang, Y. C. Zou, M. S. Dargusch, H. Wang, J. Zou, *Adv. Mater.* **2018**, *30*, 1705942.

[25] J. Li, X. Zhang, Z. Chen, S. Lin, W. Li, J. Shen, I. T. Witting, A. Faghaninia, Y. Chen, A. Jain, L. Chen, G. J. Snyder, Y. Pei, *Joule* **2018**, *2*, 976.

[26] C. Zhang, G. Yan, Y. Wang, X. Wu, L. Hu, F. Liu, W. Ao, O. Cojocaru-Mirédin, M. Wuttig, G. J. Snyder, Y. Yu, *Adv. Energy Mater.* **2023**, *13*, 2203361.

[27] Z. Zheng, X. Su, R. Deng, C. Stoumpos, H. Xie, W. Liu, Y. Yan, S. Hao, C. Uher, C. Wolverton, M. G. Kanatzidis, X. Tang, *J. Am. Chem. Soc.* **2018**, *140*, 2673.

[28] M. Hong, Y. Wang, W. Liu, S. Matsumura, H. Wang, J. Zou, Z.-G. Chen, *Adv. Energy Mater.* **2018**, *8*, 1801837.

[29] C. Zhou, Y. Yu, Y. K. Lee, O. Cojocaru-Mirédin, B. Yoo, S.-P. Cho, J. Im, M. Wuttig, T. Hyeon, I. Chung, *J. Am. Chem. Soc.* **2018**, *140*, 15535.

[30] Y. Xiao, D. Wang, Y. Zhang, C. Chen, S. Zhang, K. Wang, G. Wang, S. J. Pennycook, G. J. Snyder, H. Wu, L. D. Zhao, *J. Am. Chem. Soc.* **2020**, *142*, 4051.

[31] Q. Zhang, B. Liao, Y. Lan, K. Lukas, W. Liu, K. Esfarjani, C. Opeil, D. Broido, G. Chen, Z. Ren, *Proc. Natl. Acad. Sci. USA* **2013**, *110*, 13261.

[32] L.-D. Zhao, G. Tan, S. Hao, J. He, Y. Pei, H. Chi, H. Wang, S. Gong, H. Xu, V. P. Dravid, C. Uher, G. J. Snyder, C. Wolverton, M. G. Kanatzidis, *Science* **2016**, *351*, 141.

[33] C. Chang, M. Wu, D. He, Y. Pei, C.-F. Wu, X. Wu, H. Yu, F. Zhu, K. Wang, Y. Chen, L. Huang, J.-F. Li, J. He, L.-D. Zhao, *Science* **2018**, *360*, 778.

[34] S. Hao, F. Shi, V. P. Dravid, M. G. Kanatzidis, C. Wolverton, *Chem. Mater.* **2016**, *28*, 3218.

[35] V. F. Gustiani, L. Septiany, A. A. Nugroho, G. R. Blake, *J. Phys.: Conf. Ser.* **2019**, *1245*, 012094.

[36] L. Shaabani, S. Aminorroaya-Yamini, J. Byrnes, A. Akbar Nezhad, G. R. Blake, *ACS Omega* **2017**, *2*, 9192.

[37] X. Zhang, J. Shen, S. Lin, J. Li, Z. Chen, W. Li, Y. Pei, *J. Materiomics* **2016**, *2*, 331.

[38] A. S. Okhotin, A. N. Krestovnikov, A. A. Aivazov, A. S. Pushkarskii, *Phys. Status Solidi B* **1969**, *31*, 485.

[39] M. Cagnoni, D. Fuhren, M. Wuttig, *Adv. Mater.* **2018**, *30*, 1801787.

[40] Z. Wang, H. Wu, M. Xi, H. Zhu, L. Dai, Q. Xiong, G. Wang, G. Han, X. Lu, X. Zhou, G. Wang, *ACS Appl. Mater. Interfaces* **2020**, *12*, 41381.

[41] Z. Wang, H. Wu, B. Zhang, L. Dai, Y. Huo, Y. Huang, G. Han, X. Lu, X. Zhou, G. Wang, *Adv. Funct. Mater.* **2022**, *32*, 2111238.

[42] M. Yan, H. Geng, P. Jiang, X. Bao, *J. Energy Chem.* **2020**, *45*, 83.

[43] Z. Huang, S. A. Miller, B. Ge, M. Yan, S. Anand, T. Wu, P. Nan, Y. Zhu, W. Zhuang, G. J. Snyder, P. Jiang, X. Bao, *Angew. Chem., Int. Ed.* **2017**, *56*, 14113.

[44] M. Yan, X. Tan, Z. Huang, G. Liu, P. Jiang, X. Bao, *J. Mater. Chem. A* **2018**, *6*, 8215.

[45] S. Roychowdhury, T. Ghosh, R. Arora, U. V. Waghmare, K. Biswas, *Angew. Chem., Int. Ed. Engl.* **2018**, *57*, 15167.

[46] D. Sarkar, T. Ghosh, S. Roychowdhury, R. Arora, S. Sajan, G. Sheet, U. V. Waghmare, K. Biswas, *J. Am. Chem. Soc.* **2020**, *142*, 12237.

[47] D. Sarkar, S. Roychowdhury, R. Arora, T. Ghosh, A. Vasdev, B. Joseph, G. Sheet, U. V. Waghmare, K. Biswas, *Angew. Chem., Int. Ed.* **2021**, *60*, 10350.

[48] M. Hong, W. Lyu, Y. Wang, J. Zou, Z. G. Chen, *J. Am. Chem. Soc.* **2020**, *142*, 2672.

[49] J. Y. Raty, M. Schumacher, P. Golub, V. L. Deringer, C. Gatti, M. Wuttig, *Adv. Mater.* **2019**, *31*, 1806280.

[50] M. Wuttig, V. L. Deringer, X. Gonze, C. Bichara, J. Y. Raty, *Adv. Mater.* **2018**, *30*, 1803777.

[51] A. Otero-de-la-Roza, E. R. Johnson, V. Luaña, *Comput. Phys. Commun.* **2014**, *185*, 1007.

[52] M. Kohout, DGrid, version 4.7, Radebeul, Germany **2019**.

[53] R. F. W. Bader, M. E. Stephens, *J. Am. Chem. Soc.* **1975**, *97*, 7391.

[54] B. J. Kooi, M. Wuttig, *Adv. Mater.* **2020**, *32*, 1908302.

[55] G. N. Lewis, *J. Am. Chem. Soc.* **1916**, *38*, 762.

[56] S. Maier, S. Steinberg, Y. Cheng, C. F. Schon, M. Schumacher, R. Mazzarello, P. Golub, R. Nelson, O. Cojocaru-Miredin, J. Y. Raty, M. Wuttig, *Adv. Mater.* **2020**, *32*, 2005533.

[57] M. Zhu, O. Cojocaru-Miredin, A. M. Mio, J. Keutgen, M. Kupers, Y. Yu, J. Y. Cho, R. Dronskowski, M. Wuttig, *Adv. Mater.* **2018**, *30*, 1706735.

[58] C.-F. Schön, S. van Bergerem, C. Mattes, A. Yadav, M. Grohe, L. Kobbelt, M. Wuttig, *Sci. Adv.* **2022**, *8*, eade0828.

[59] R. Arora, U. V. Waghmare, C. N. R. Rao, *Adv. Mater.* **2022**, *35*, 2208724.

[60] M. Wuttig, C.-F. Schön, J. Lötfering, P. Golub, C. Gatti, J.-Y. Raty, *Adv. Mater.* **2022**, 2208485, https://doi.org/10.1002/adma.202208485.

[61] X. Li, Z. Liang, J. Li, F. Cheng, J. He, C. Zhang, J. Li, F. Liu, T. Lyu, B. Ge, L. Hu, *Nano Energy* **2022**, *100*, 107434.

[62] B. Gault, A. Chiaramonti, O. Cojocaru-Mirédin, P. Stender, R. Dubosq, C. Freysoldt, S. K. Makineni, T. Li, M. Moody, J. M. Cairney, *Nat. Rev. Methods Primers* **2021**, *1*, 51.

[63] Y. Cheng, O. Cojocaru-Miredin, J. Keutgen, Y. Yu, M. Kupers, M. Schumacher, P. Golub, J. Y. Raty, R. Dronskowski, M. Wuttig, *Adv. Mater.* **2019**, *31*, 1904316.

[64] C. Rodenkirchen, M. Cagnoni, S. Jakobs, Y. Cheng, J. Keutgen, Y. Yu, M. Wuttig, O. Cojocaru-Mirédin, *Adv. Funct. Mater.* **2020**, *30*, 1910039.

[65] L. Yao, B. Gault, J. M. Cairney, S. P. Ringer, *Philos. Mag. Lett.* **2010**, *90*, 121.

[66] L. Guarneri, S. Jakobs, A. von Hoegen, S. Maier, M. Xu, M. Zhu, S. Wahl, C. Teichrib, Y. Zhou, O. Cojocaru-Miredin, M. Raghuwanshi, C. F. Schon, M. Drogeler, C. Stampfer, R. Lobo, A. Piarristeguy, A. Pradel, J. Y. Raty, M. Wuttig, *Adv. Mater.* **2021**, *33*, 2102356.

[67] H. Wang, Y. Pei, A. D. LaLonde, G. J. Snyder, *Proc. Natl. Acad. Sci. USA* **2012**, *109*, 9705.

[68] Z. M. Gibbs, F. Ricci, G. Li, H. Zhu, K. Persson, G. Ceder, G. Hautier, A. Jain, G. J. Snyder, *npj Comput. Mater.* **2017**, *3*, 8.

[69] R. Wu, Y. Yu, S. Jia, C. Zhou, O. Cojocaru-Miredin, M. Wuttig, *Nat. Commun.* **2023**, *14*, 719.

[70] Y. Yu, M. Wuttig, *Nano Res. Energy* **2023**, *2*, 9120057.

[71] S. Lee, K. Esfarjani, T. Luo, J. Zhou, Z. Tian, G. Chen, *Nat. Commun.* **2014**, *5*, 3525.

[72] K. Yuan, Z. Sun, X. Zhang, X. Gong, D. Tang, *Phys. Chem. Chem. Phys.* **2020**, *22*, 1911.

[73] Y. Zhang, X. Ke, C. Chen, J. Yang, P. R. C. Kent, *Phys. Rev. B* **2009**, *80*, 024304.

[74] M. K. Brod, M. Y. Toriyama, G. J. Snyder, *Chem. Mater.* **2020**, *32*, 9771.

[75] D. S. Parker, A. F. May, D. J. Singh, *Phys. Rev. Appl.* **2015**, *3*, 064003.